Understanding Bulk Defects in Topological Insulators from Nuclear-Spin Interactions

*Dimitrios Koumoulis, Belinda Leung, Thomas C. Chasapis, Robert Taylor, Daniel King Jr., Mercouri G. Kanatzidis, and Louis-S. Bouchard**

Non-invasive local probes are needed to characterize bulk defects in binary and ternary chalcogenides. These defects contribute to the non-ideal behavior of topological insulators. The bulk electronic properties are studied via ^{125}Te NMR in Bi_2Te_3, Sb_2Te_3, $Bi_{0.5}Sb_{1.5}Te_3$, Bi_2Te_2Se, and Bi_2Te_2S. A distribution of defects gives rise to asymmetry in the powder lineshapes. The Knight shift, line shape, and spin-lattice relaxation are investigated in terms of how they affect carrier density, spin-orbit coupling, and phase separation in the bulk. The present study confirms that the ordered ternary compound Bi_2Te_2Se is the best topological insulator candidate material at the present time. These results, which are in good agreement with transport and angle-resolved photoemission spectroscopy studies, help establish the NMR probe as a valuable method to characterize the bulk properties of these materials.

1. Introduction

The band structure of V_2VI_3 layer-type semiconductors offers a desirable platform for thermoelectric (TE) and topological insulating properties.[1–39] Prototype TE and topological insulating compounds of interest in applications include antimony telluride (Sb_2Te_3) and bismuth telluride (Bi_2Te_3).[7–11,20–22,26–32] These binary chalcogenides have been extensively studied due to their large thermo-electric power and applications as solid state power generators and refrigerators (Peltier, Seebeck and Thomson devices).[20–22,26–29] Recently, an effort aimed at improving the TE efficiency (Figure of merit parameter, *ZT*) concluded that Bi_2Te_3-Sb_2Te_3 solid solutions yield improved TE materials, according to the *ZT* parameter, which is maximized in the case of $Bi_{0.5}Sb_{1.5}Te_3$[7,17–20,24–29] Other ternary telluride compounds in the same class as these layered materials, Bi_2Te_2Se and Bi_2Te_2S, have shown the potential of tuning and enhancing transport properties.[1–6,30,32]

Dr. D. Koumoulis, B. Leung, Dr. R. Taylor, D. King Jr., Prof. L.-S. Bouchard
Department of Chemistry and Biochemistry
California NanoSystems Institute
607 Charles Young Drive East
University of California
Los Angeles, 90095, USA
E-mail: bouchard@chem.ucla.edu
Dr. T. C. Chasapis, Prof. M. G. Kanatzidis
Department of Chemistry and Biochemistry
Northwestern University
Evanston, IL, USA

DOI: 10.1002/adfm.201302673

The discovery of topological insulators has changed the way we look at chalcogenides.[11–16] An ideal topological insulator (TI) has a bulk interior characterized by an insulating bandgap, while the boundary exhibits gapless Dirac-like edge (2D-TIs) or surface states (3D-TIs).[11–16,36–43] Experimental realizations of TIs to date have used narrow bandgap materials with strong spin-orbit coupling (SOC) featuring a helical surface band structure with spin locked to momentum. The observation of metallic surface states often requires minimal bulk defects or compensation for the free carriers.[1–6,11,14,37–53] Novel properties have been predicted, such as quantum-Hall-like behavior with quantized conductance of charge and spin in the absence of a magnetic field, and dissipation-less quantum Hall states with time-reversal symmetry (TRS).[11–16] First-principles calculations[3,15,16,33,36–40,48,49,51] and angle resolved photoemission spectroscopy (ARPES)[5,11,12,39–41,51] results have yielded energy band structures of most binary and ternary chalcogenides.

The characterization of TI states requires sensitive techniques to probe metallicity of the surface state, because the surface is where the interesting properties are found.[11] To date, electrical transport measurements, scanning tunneling microscopy (STM) and ARPES have been the main workhorses for the study of surface states.[1–6,11,13,40–43] These techniques work best with high-quality thin films (<20 nm)[40–43] or large single crystals and at low temperatures (<30 K).[1–6,11,39,42,43] There is, however, a need for characterizing materials at room temperature or materials of suboptimal quality. To this end, nuclear magnetic resonance (NMR) has been proposed as a tool to characterize TI properties.[54–57] NMR is a non-invasive local probe of magnetism and electronic wavefunction in narrow-gap semiconductors.[54–61] It has been used to study the bulk semiconductor properties of chalcogenides,[47,54–57] as well as the properties of TI nanoparticles.[54] Worthwhile aspects of the NMR readout include: (i) potential operation at higher temperatures and ambient conditions, (ii) ability to probe lower quality or amorphous materials, (iii) study of "granular" varieties and (iv) materials with a large number of bulk defects with topologically protected gapless modes.[54–57,59,61] Magnetic resonance techniques could serve as a complementary tool to characterize materials which are not suitable for study by conventional methods (transport, ARPES, STM). Of great interest is the development of local probes of the material's bulk region,

which is difficult to interrogate independently from the surface states.[52,53] Here we present a comparative NMR study of the bulk states of multiple TI materials and relate the results to existing transport and ARPES studies from the literature. The present study confirms that the undesired presence of defects in the bulk state are directly reflected in the NMR parameters.

2. Material Properties

Bi_2Te_3, Sb_2Te_3 and Bi_2Se_3 are the simplest members of the Tetradymite family, which are crystallized in the primitive rhombohedral structure belonging to the $D_{3d}^5\ (R\bar{3}m)$ space group. Their structure is arranged in quintuple layers stacked upon each other along the c-axis, separated by van der Waals gaps. For Bi_2Te_3 and Sb_2Te_3, for example, the layers are arranged in the following way: Te(2)-Bi-Te(1)-Bi-Te(2) and Te(2)-Sb-Te(1)-Sb-Te(2), respectively, where the labels (1) and (2) denote crystallographically different sites. The Te(2) sites refer to the outer planes of the quintuples which are exposed to the van der Waals gaps and host the topological surface states.[6–9,16–30]

The type of conduction in the Tetradymite family of TIs is strongly related to the type of structural defects present (anion vacancies or antisite).[1–14,16,22,25,28,32,35] Bi_2Te_3 crystals grown from stoichiometric melts are *p*-type due to the presence of large number of Bi_{Te} antisite defects. The type of conduction may be adjusted through fine tuning of the non-stoichiometry of the Bi/Te ratio, i.e., to dope the system by generating antisite defects of Bi_{Te} (*p*-type) or Te_{Bi} (*n*-type).[18] The most common defects in Sb_2Te_3 are the Sb_{Te} antisite defects, giving rise to large *p*-type conduction.[6,10,21,23] The presence of weak bond pol arity[3,6,9,23,25,26,29,32,35,39,62–64] (difference in electronegativity) is a key parameter that explains the formation of antisite defects in these materials. Even a small discrepancy in stoichiometry or dopants mixed into the Tetradymite matrix can affect the initial polarity of the bonds, leading to antisite defects.[8,10,13,20,45,62–65] Bi_2Se_3, as prepared, is observed to be *n*-type owing to a large number of Se vacancies formed at the chalcogen outer layers due to evaporation.[6,19] Recently, Bi_{Se} antisite and partial Bi_2-layer intercalation defects were also identified in stoichiometric and non-stoichiometric Bi_2Se_3.[14]

A common route to optimize TI material properties involves alloying of the binary starting materials. Alloying offers two degrees of freedom: tuning the carrier density, i.e. the position of the Fermi level, and/or moving the Dirac point relative its position in the parent binary compound. Given the similarities in crystal structure and lattice constants, ternary compounds of the type $(Bi_{1-x}Sb_x)Te_3$ were proposed to tailor the Dirac point and provide charge compensation by adjusting the Bi/Sb stoichiometry. Bi_2Te_3 has an indirect bandgap equal to 0.16 eV and its Dirac point lies in the valence band.[5,18,22,26,27,31,45,47,56] **Figure 1**a compares ARPES band structures of (1) Bi_2Te_3, (3) $Bi_{0.5}Sb_{1.5}Te_3$ and (4) Sb_2Te_3, along the symmetry paths K-Γ-M and M-Γ-M in the first Brillouin zone, where the Dirac point is clearly more exposed in the case of the solid solution (3) relative to the parent binary Bi_2Te_3.[5,36,37,40] In $Bi_{0.5}Sb_{1.5}Te_3$ (direct bandgap, 0.2 eV), the Sb dopant alters the initial density of defects but keeps the bulk carrier density constant without affecting the TI surface states.[16,20,21,24,25,40,41] Recently, in situ ARPES results have shown that as the Bi/Sb ratio approaches 0.25/0.75, the Fermi energy shifts to the bulk valence band (BVB) leading to a hybrid state consisting of the surface state band (SSB) and the BVB pocket.[40,41,48]

Alloying two parts of Bi_2Te_3 for each part of Bi_2Se_3 forms the structurally ordered Bi_2Te_2Se phase [i.e., 66.7% Bi_2Te_3 with 33.3% Bi_2Se_3], where Se atoms being trapped between two Bi atoms and the basic quintuple-layer unit being Te-Bi-Se-Bi-Te. The phase was found with *n*-type conduction and high bulk resistivity at low temperatures, 1 Ω·cm.[4,5] The low carrier concentration originates from a compensation mechanism

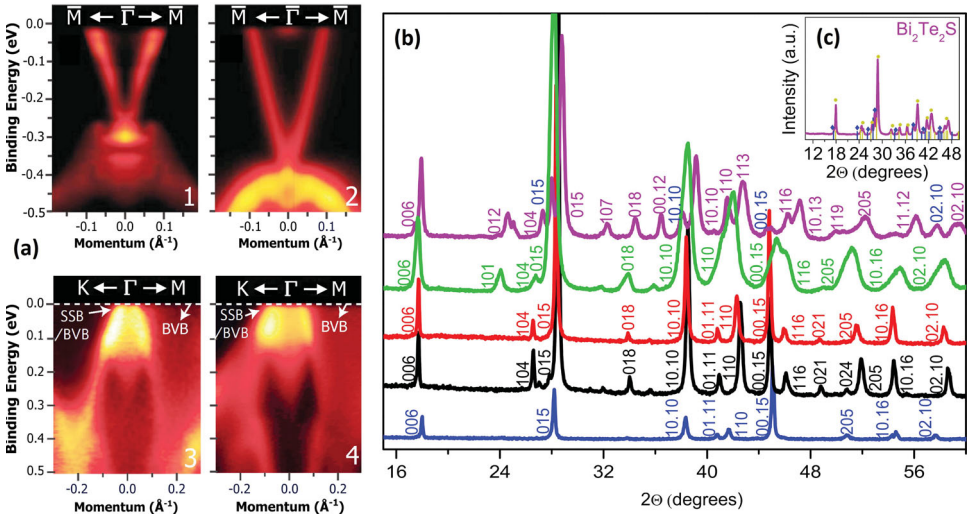

Figure 1. Comparison of ARPES results (a) of the band structures of (1) Bi_2Te_3 and (2) Bi_2Te_2Se, (3) $Bi_{0.5}Sb_{1.5}Te_3$, (4) Sb_2Te_3, along the K-Γ-M and M-Γ-M symmetry momentum directions (a). PXRD patterns from mortar and pestle powders Bi_2Te_3 (blue), $Bi_{0.5}Sb_{1.5}Te_3$ (red), Sb_2Te_3 (black), Bi_2Te_2S (purple) and Bi_2Te_2S (green) at room temperature (b). PXRD patterns of all the samples confirm their crystallinity. Bi_2Te_2S is a macroscopically phase separated TI with one of the phases being S-poor Bi_2Te_3 and the second one, $Bi_2Te_{2+\delta}S_{1-\delta}$ (c). [ARPES images 1 and 2 (top row) adapted with permission.[5] Copyright 2012, APS; images 3 and 4 (bottom row) adapted with permission.[40] Copyright 2011, Nature.

Table 1. Structural and transport parameters obtained from PXRD and NMR analysis. For the Bi_2Te_2S the lattice parameters are referred to the S-poor and S-rich phases. The carrier concentration (N) for Bi_2Te_3, $Bi_{0.5}Sb_{1.5}Te_3$ and Sb_2Te_3 are based on literature data. The N values for the Bi_2Te_2Se and Bi_2Te_2S were determined from Hall measurements of the present study.

Composition	Lattice parameters [Å]				Volume [Å^3]		Activation energy [kJ/mol]		Carrier concentration [cm^{-3}]	$1/(T_1 \cdot T^{0.5}) \propto N$ [s$^{-1}\cdot$K$^{1/2}$]
	α		c		V		Low T[a)]	High T[b)]	N	
Bi_2Te_3[c)]	4.322		29.535		477.888		2.26	8.44	(1-5) $\cdot 10^{19}$	0.76
$Bi_{0.5}Sb_{1.5}Te_3$[d)]	4.268		30.134		473.512		4.89		(4-7) $\cdot 10^{19}$	3.05
Sb_2Te_3[e)]	4.239		30.034		467.542		0.68	5.63	(3-8) $\cdot 10^{19}$	2.83
Bi_2Te_2Se[f)]	4.292		30.111		480.580		5.20	13.60	$8.55\cdot 10^{18}$	0.10
Bi_2Te_2S[f)]	4.349	4.226	30.487	29.500	499.300	456.210	2.50	5.40	$1.82\cdot 10^{19}$	0.20

[a)]Temperature range below 270 K; [b)]Temperature range above 270 K; [c)]Reference [10,11,34,35,43]; [d)]Reference [10]; [e)]Reference [10,21,23,25,35]; [f)]Current study.

between Bi_{Te} antisites and Te vacancies which dope holes and electrons respectively, while the Se vacancies are suppressed relative to the Bi_2Se_3 because the Se atoms trapped between two Bi atoms are less exposed to evaporation.[1] Considering that Bi_2Se_3 has the Dirac point of the surface states at an energy well separated from the energies of the top of the bulk valence band and the bottom of the bulk conduction band, the Dirac point energy of the Bi_2Te_2Se shown in (2) of Figure 1a, appears at a higher energy than in Bi_2Te_3.[2,4–6,40] Although Bi_2Te_2Se is one of the most important compositions for studying the surface quantum transport in a topological insulator,[1–6] its Dirac point appears to be near the energy of the top of the valence band, suggesting that the bulk states will interfere with surface states conductivity. By replacing the element Se with the more electronegative S in Bi_2Te_2Se, the absolute energy of the valence band is expected to decrease below the Dirac point.[6] Recently, a S-rich $Bi_2Te_{2-x}S_{1+x}$ composition has been the subject of investigation as the host for topological surface states. In particular, the n-type $Bi_2Te_{1.6}S_{1.4}$ which incorporates both S and Te in its outer chalcogen layers has shown that the layers supporting the surface states are randomly corrugated on the atomic scale, while partial substitution of Sb for Bi yielded a high resistivity material with well isolated Dirac point[5] According to ARPES results and ab initio calculations,[1–6,37,39] Bi_2Te_2S as well as Bi_2Te_2Se exhibit striking similarities with Bi_2Te_3. Defects are found both on the surface and the bulk of these TIs.[1–6,39]

The defect density in the all Tetradymite TIs is strongly dependent on growth method used for synthesis and the form of the final material (single crystals, thin films, nanocrystals, etc.). These factors, in turn, determine the actual carrier concentrations.[1–6,22–26,40,41] ARPES and STM measurements are excellent probes of TI surface defects. However, they cannot easily probe antisite defects and vacancies in the bulk, whose properties are different than on the surface. In any case, this study explores NMR techniques as a complementary characterization tool to overcome some of the limitations associated with probing the bulk.

3. Results and Discussion

Figure 1b shows the powder XRD patterns of the studied compositions. The patterns for all the samples can be well indexed with the rhombohedral structure where the 015 reflection of the hexagonal unit cell is the strongest, confirming that the ternaries compositions maintain the same crystal structure as the binaries counterparts. Based on the PXRD spectra, the materials are single phase materials except for the Bi_2Te_2S which was found phase separated. This is actually supported by the comparison of the respective PXRD pattern with the pure Bi_2Te_3 and Bi_2Te_2S reflections shown in Figure 1c. The experimental pattern is well described by taking into account the contribution of two phases. As can be seen from Figure 1c, the PXRD peaks at ~28° and ~29°, attributed to the 015 reflections of the two hexagonal phases, are blue shifted relative to the pure compounds indicating that the material may be regarded as being composed by a S-poor and a S-rich Bi_2Te_3 compositions, with the latter having the strongest contribution.

The lattice constants and the volume of the hexagonal unit cell are obtained after refinement of the respective PXRD spectra and are tabulated in **Table 1**. The values lie close to the literature values. For the phase separated composition the refinement based on the two pure phases yielded two pairs of in-plane, out-of plane lattice constants; 4.349Å, 30.487Å, 4.226Å, and 29.500Å. The first pair is attributed to the S-poor constituent. Based on the lattice constants of the pure Bi_2Te_2S, 4.239Å, 29.576Å, we may conclude that the composition of the second phase is $Bi_2Te_{2+\delta}S_{1-\delta}$. Regarding the carrier concentrations it is evident from Table 1 that the Bi_2Te_2Se composition shows the lowest value in the range of 10^{18} cm^{-3} supporting the idea that the ordered phase is the most promising TI.

^{125}Te NMR spectra of Bi_2Te_3, $Bi_{0.5}Sb_{1.5}Te_3$, Sb_2Te_3, Bi_2Te_2Se, and Bi_2Te_2S at temperatures in the range 170-423 K are shown in **Figure 2**. The resonance line shapes of Sb-TIs are clearly asymmetric, especially in the case of $Bi_{0.5}Sb_{1.5}Te_3$. Such asymmetrical features arise predominantly from interactions of nuclear moments with conduction band carriers.[54,55,59–61] In prior studies of Bi_2Se_3 and Bi_2Te_3, the asymmetric resonance lines were attributed to an inhomogeneous distribution of defects in a low symmetry rhombohedral space group environment yielding different charge carrier concentrations in different crystalline regions, resulting in a range of Knight shifts.[54,55] A spectral model for the Sb-TI samples and the phase separated Bi_2Te_2S is a sum of two Lorentzians. For Bi_2Te_3 and Bi_2Te_2Se, the line shapes are more symmetric and are well described by a single Lorentzian line.

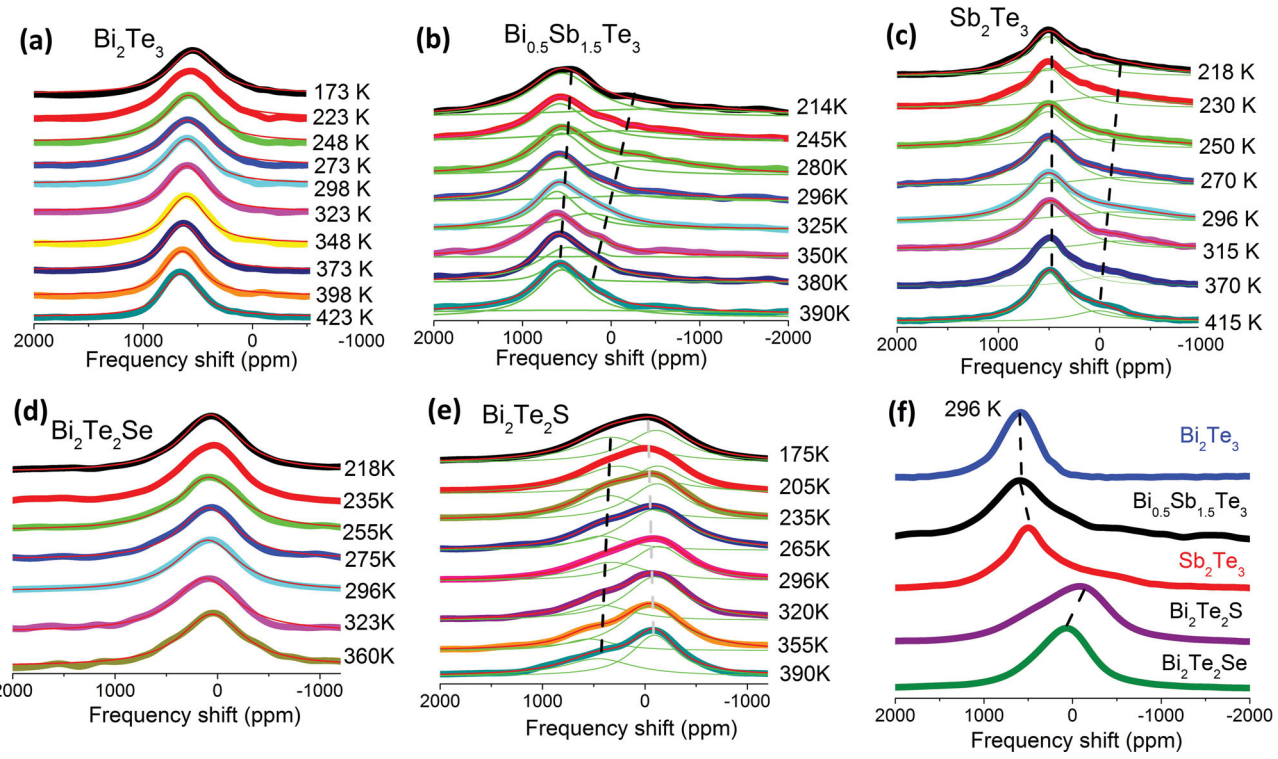

Figure 2. ^{125}Te NMR powder spectra for (a) Bi_2Te_3, (b) $Bi_{0.5}Sb_{1.5}Te_3$, (c) Sb_2Te_3, (d) Bi_2Te_2Se and (e) Bi_2Te_2S as a function of temperature. The red thin lines are multi-component best fits, and the green thin lines are the individual components. A comparative plot (d) of NMR powder spectra at 296 K indicates a negative frequency shift as the Sb concentration increases in the case of the *p*-type materials and a positive frequency shift for the *n*-type TIs. The Bi_2Te_2S as a phase separated (Bi_2Te_3-$Bi_2Te_{2+\delta}S_{1-\delta}$) material reveals a left shoulder peak (e). The left shoulder peak is attributed to the Bi_2Te_3-rich phase since it has equal frequency shift with Bi_2Te_3 (f).

From the data of Figure 2 we extracted center frequency and linewidth of each Lorentzian line (for both central and shoulder peaks) and summarized the results as function of temperature in **Figure 3**. We observe the following features: 1) the NMR shift of central peaks of Bi_2Te_3 and $Bi_{0.5}Sb_{1.5}Te_3$ become more negative (lower frequency) with decreasing temperature, except for Sb_2Te_3, Bi_2Te_2Se and Bi_2Te_2S which remain essentially constant within experimental uncertainty. 2) In all cases, the NMR shift of the shoulder peaks exhibits a strong temperature dependence. Furthermore, this temperature dependence of the NMR shift is more pronounced at low temperatures in the case of $Bi_{0.5}Sb_{1.5}Te_3$, suggesting an increase in carrier density. Knight shifts in narrow-band multi-valley semiconductors (Equation 1) have been explained previously in terms of SOC.[44–47,55–61,68] One of the defining features of such Knight shifts is their temperature dependence, which gravitates toward more negative frequencies as temperature decreases, owing to the temperature dependence of the energy gap.[44–47,55–59] According to the theory,[44–47] the Knight shift can be expressed as,

$$K = \zeta \frac{8\pi}{3} \gamma_e^2 h^2 \left\langle |u_k(0)|^2 \right\rangle_{E_0} \frac{n_e}{kT}, \quad (1)$$

where γ_e is the electron magnetogyric ratio, h is Planck's constant, n_e is the carrier density, $\left\langle |u_k(0)|^2 \right\rangle_{E_0}$ is the free electron density near the bottom of the conduction band for electrons or near the top of the valence band for holes and ζ is a numerical factor close to unity which depends on the origin and strength of the hyperfine interaction (Fermi contact, dipolar or orbital). The observed ^{125}Te Knight shift unveils different bulk electronic states and density of states at the Fermi level in the present TIs, which we attribute to large differences in defect and vacancy concentration. Transport, ARPES and structural studies in the same materials[1–6,11,16,37,41–43,69,70] are in agreement and support the above NMR Knight shift behavior.

A plot of linewidth as function of temperature is shown in Figure 3b. As mentioned previously, the linewidth in these samples reflects an inhomogeneous distribution of native defects with an increased carrier density having different Knight shifts.[47,54–56,58–61] A previous NMR study on Bi_2Se_3[56] reported a narrower spectral linewidth in samples with lower defect concentration, which is in agreement with our study of all present TIs. We identify that the temperature dependence of the linewidth in all the samples is different (Figure 3c). In addition, we note that as the temperature decreases, the linewidth for the ternary compound $Bi_{0.5}Sb_{1.5}Te_3$ is larger compared to the binary TIs. The $Bi_{0.5}Sb_{1.5}Te_3$ linewidth is more than 300 ppm larger than that of Bi_2Te_3 near 215 K. Although the five materials share the same rhombohedral structure, a different defect level gives rise to the observed difference of the temperature dependent linewidths. This is due to the increased broadening via spin-flip scattering events by the charge carriers in the bulk,[54–61] which are found to be at a higher concentration in the case

of $Bi_{0.5}Sb_{1.5}Te_3$ due to the higher density of defects.[8–11,64,69,70] Indeed, recent ^{209}Bi NMR results on Bi_2Se_3 with different defect levels show a significant difference in linewidths, which was attributed to different amounts of charge carriers.[56] Another interesting feature we observe with all these TIs is that the linewidth of the shoulder peak decreases with increasing temperature, as would be expected due the motional narrowing of the lineshapes accompanied with a lack of annealing of the native defects at higher temperatures.[54,55,58–61,68] Dislocations, strains and vacancies in the lattice can also enhance the observed line broadening, e.g., due to the substitution of Sb or S in the Bi_2Te_3 matrix, especially in the case of the solid-solution $Bi_{0.5}Sb_{1.5}Te_3$[10,17,24,26,28,33,35] and Bi_2Te_2S (a phase separated material).[5,6,71,72]

^{125}Te spin-lattice relaxation in materials which are dominated by structural defects is best described with a stretched exponential model (Kohlrausch function)[54,55,57,59–61,73]

$$M(t) = M_0\left(1 - \exp\left(-\frac{t}{T_1}\right)^{\beta}\right), \quad (2)$$

where T_1 is the spin-lattice relaxation time and β is the Kohlrausch exponent. For $Bi_{0.5}Sb_{1.5}Te_3$ and Sb_2Te_3, $\beta = 0.5$ and $\beta = 0.9$, respectively, provided a good fit, whereas $\beta = 1$ (single exponential) gave a better fit for Bi_2Te_3. With Bi_2Te_2S and Bi_2Te_2Se, $\beta = 0.7$ provided the better fit. Typical T_1 saturation recovery curves for Sb-TIs, Bi_2Te_2S and Bi_2Te_2Se are shown in **Figure 4** (see also reference [55] for Bi_2Te_3). As shown in Figure 4 insets for all cases the β has a temperature independent behavior and thus the T_1 does not change its overall behavior across the entire temperature range since there is a constant underlying distribution in T_1. In order to avoid unnecessary experimental scattering in the T_1 process, we return back and fit again all the saturation recovery data to Equation 2 using the best fixed value of β. The stretched exponential has been used for many decades to model NMR relaxation characterized by a distribution of relaxation rates in materials such as semiconductors. The β exponent is a measure of the width of the $1/T_1$ distribution.[57] Recently, another detailed ^{209}Bi NMR study by Nisson et al. on single crystal TI materials (Bi_2Se_3, Bi_2Te_2Se) conclude that the T_1 recovery data fits better to the stretched exponential model.[57]

The natural logarithm of the spin-lattice relaxation rate as a function of the inverse temperature, obtained from the fitting results, is shown in **Figure 5**a. The binary chalcogenides follow a two-channel relaxation process, whereas the results of $Bi_{0.5}Sb_{1.5}Te_3$ follow a single relaxation mechanism across the entire temperature region (170-423 K). In the case of Bi_2Te_3 and Sb_2Te_3, the first relaxation mechanism occurs in the low temperature regime (<270 K) and follows a thermal activation process with an activation energy of about 2.26 kJ/mol (23 meV) for Bi_2Te_3 and 0.68 kJ/mol (7 meV) in case of Sb_2Te_3. Above 270 K, another relaxation mechanism becomes apparent, which is characterized by an activation energy of 8.44 kJ/mol (87 meV) for Bi_2Te_3 and 5.13 kJ/mol (53 meV) for Sb_2Te_3. This high temperature process is typical of semiconductors with nuclear spins that interact with thermally activated charge carriers. The $Bi_{0.5}Sb_{1.5}Te_3$, on the other hand, exhibits an Arrhenius behavior across the entire temperature region with activation energy equal to 4.89 kJ/mol (51 meV). While these values for the activation energy (reflect inter-band excitations and not to be confused with the bandgap between the valence and conduction band) should not be taken too literally given the narrow range of temperatures investigated, the analysis does allow for the identification of distinct relaxation mechanisms. We also note that there is no significant energy difference at the high temperature regime between Sb_2Te_3 and $Bi_{0.5}Sb_{1.5}Te_3$. However, the low temperature relaxation mechanism does not present itself in the relaxation process for $Bi_{0.5}Sb_{1.5}Te_3$. A further analysis by a power-law fit ($1/T_{1\propto}T^n$) of relaxation rates (Figure 5d) confirms the existence of a slow temperature dependence of the form $1/T_{1\propto}T^{0.3}$ for Sb_2Te_3 and a $1/T_{1\propto}T^{1.2}$ for Bi_2Te_3 below 270 K, whereas a Raman-type process is likely to govern all the samples above 270 K, as evidenced by the $T^{n \geq 2}$ dependence of two-phonon relaxation processes. The Raman relaxation mechanism involving the interactions between nuclear spins and lattice vibrations is also active in the case of spin-*1/2* nuclei (such as ^{125}Te, ^{207}Pb, ^{77}Se, ^{119}Sn, etc.). Especially in case of ^{125}Te and ^{77}Se NMR, the existence of Raman process has been known since the 1970s.[78–81] The above view is supported by the observation of a temperature-dependent T_1 relaxation process proceeding by the inelastic scattering of phonons by the spin (Raman mechanism). Recently, an unusual

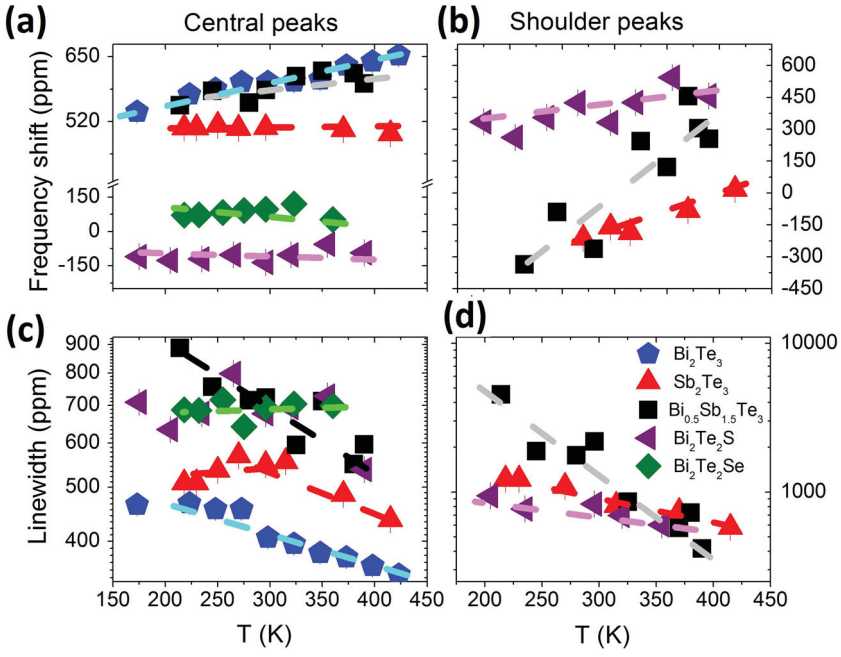

Figure 3. Temperature dependence of the frequency shift (a,b) and linewidth (c,d) for Bi_2Te_3 (⬟), Sb_2Te_3 (▲, central and shoulder peak), $Bi_{0.5}Sb_{1.5}Te_3$ (■, central and shoulder peak), Bi_2Te_2Se (◆) and Bi_2Te_2S (◀, central and shoulder peak).

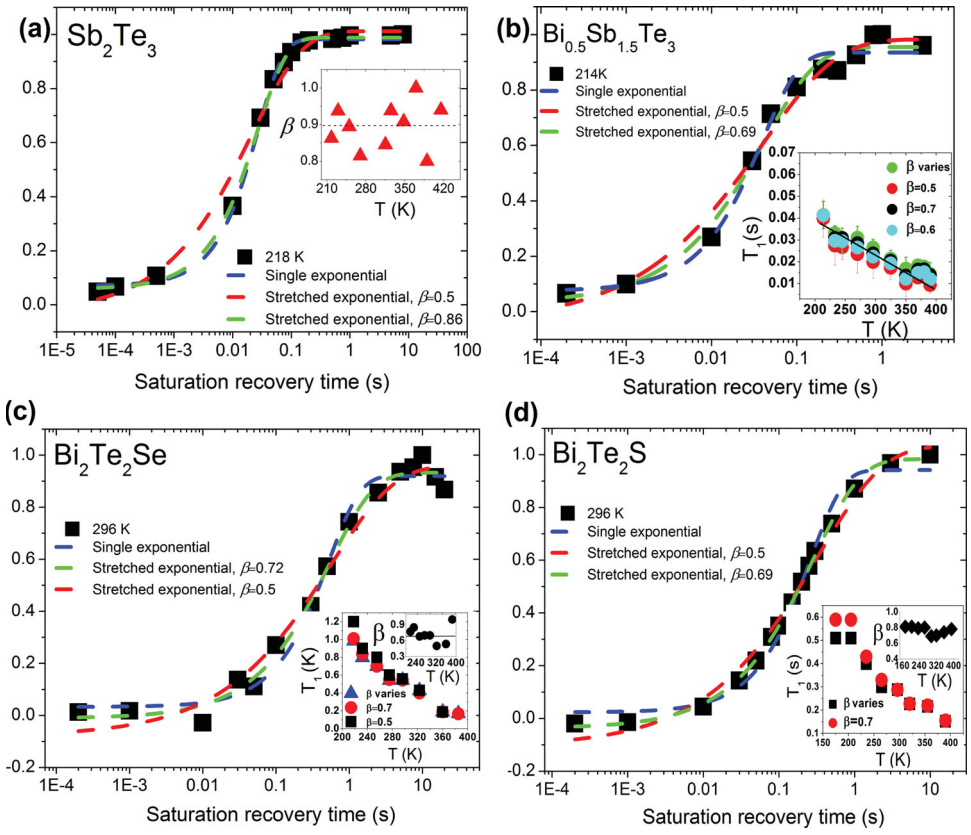

Figure 4. Spin-lattice saturation recovery (T_1) relaxation data of the entire resonance for (a) Sb_2Te_3 whereas the inset presents the temperature dependence of β. (b) $Bi_{0.5}Sb_{1.5}Te_3$ and the inset reveals that the β does not affect the overall trend of T_1. Bi_2Te_2Se at 296K and the $T_1\beta$-independence across the temperature range (c) and (d) Bi_2Te_2S (296 K). The blue dashed line shows a fit of a single exponential ($\beta = 1$), the red ($\beta = 0.5$) and green (by allowing the β parameter to vary) dashed lines the fits with stretched exponential.

power-law dependence of the electrical resistivity and Raman measurements in the temperature range 20-270 K has been observed in the case of binary TIs (Sb_2Te_3 and Bi_2Te_3) accompanied by an anomalous thermal expansion in the temperature range 221–228 K.[65,75–77]

The Bi_2Te_2Se and Bi_2Te_2S behave much like Bi_2Te_3 throughout the entire temperature range, but due to lower bulk conductivities, exhibit higher activation energies. These NMR results are in agreement with ab initio, magneto-transport and ARPES results.[1–6] Bi_2Te_2Se and Bi_2Te_2S feature a higher bulk insulating behavior compared to Bi_2Te_3 and Bi_2Se_3 as a result of a decrease in the SOC strength and limited antisite Bi-Te and Se vacancies, which in turn, is expected to result in longer relaxation times. This is reflected in our NMR results of Figure 5. Additionally, based on recent ab initio calculations,[37] the SOC constant in Bi_2Te_2Se is two times weaker than in Bi_2Te_2S, Bi_2Te_3 and Bi_2Se_3. The SOC contribution to the spin-lattice relaxation in TI materials has also been observed in a previous NMR study on Bi_2Se_3 and Bi_2Te_3.[55]

It is interesting to compare the above results on TIs with a recent ^{125}Te NMR study of PbTe, a narrow-gap semiconductor (0.32 eV) which is not a TI.[61] PbTe exhibits an activation energy of approximately 15.36 kJ.mol^{-1} (159 meV) (nearly three times larger than that found for all the above TIs) in the higher temperature regime, and a second relaxation mechanism at lower temperatures characterized by an activation energy of 6.05 kJ.mol^{-1} (63 meV), nearly seven times larger than that found for all the above TIs. The smaller activation energy of TIs is attributed to excitations of electrons from impurity band states (defect or vacancy localized states) which lie above the valence band into the conduction band.[55] The strong temperature-dependent relaxation mechanism, especially in the case of binary TIs, is attributed to the presence of an indirect bandgap. A strong electron (or hole)–phonon coupling associated with changes in the bonding lengths[1–6,10,35,37,65,71,72,74–77,82] (Bi-Te, Sb-Te, Te-Se,Te-S) can account for this effect, as has already been observed in the case of another chalcogenide ($MoSe_2$).[74] In this system, thermal excitation across an indirect bandgap requires the addition of a phonon-assisted mechanism (associated with a change in crystal momentum) in the first Brillouin zone. [10,22,74]

The temperature dependence of the Korringa product[59] T_1.T for all samples is shown in Figure 5b. A lower value of the T_1.T means a higher density of states at the Fermi level ($D^2(E_F)$), since $1/T_1.T \sim D^2(E_F)$, leading to a more conductive bulk.[55–61] The lowest Korringa products across all temperatures are associated with $Bi_{0.5}Sb_{1.5}Te_3$ and Sb_2Te_3, which implies that $D^2(E_F)$ is higher compare to the other TIs. On the other hand, Bi_2Te_3 reveals a Korringa law below 200 K and a semiconducting behavior at high temperatures. A critical parameter that affects

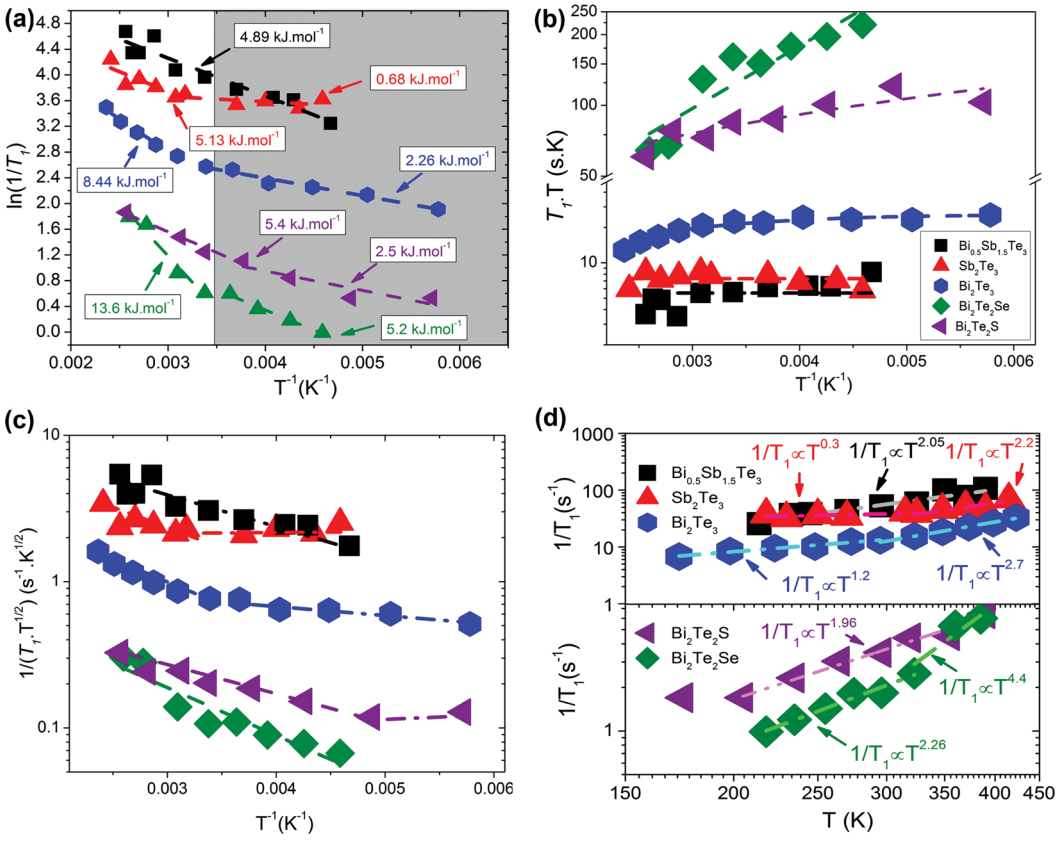

Figure 5. The natural logarithm of the ^{125}Te spin-lattice relaxation rate in the case of $Bi_{0.5}Sb_{1.5}Te_3$ (■), Sb_2Te_3 (▲), Bi_2Te_3 (⬟), Bi_2Te_2S (◀) and Bi_2Te_2Se (◆) as a function of the inverse temperature (a). Below 270 K, a second mechanism dominates the spin-lattice relaxation. Comparison of the Korringa product (b) of the ^{125}Te spin-lattice relaxation time with the temperature as a function of the inverse temperature for $Bi_{0.5}Sb_{1.5}Te_3$ (■), Sb_2Te_3 (▲), Bi_2Te_3 (⬟), Bi_2Te_2S (◀) and Bi_2Te_2Se (◆) m&p samples. A semi-logarithmic plot for $1/(T_1.T^{0.5})$ vs inverse temperature of the three TIs. The quantity $1/(T_1.T^{0.5})$ is proportional to charge carrier concentration (see text and Table 1). The temperature dependence of the spin-lattice relaxation rate for all the samples (d). The dashed lines show power-law fit ($1/T_{1\propto}T^n$) of relaxation rates. The power law fit gives a slow temperature dependence of the form $1/T_{1\propto}T^{0.3}$ only for the Sb_2Te_3 and a $1/T_{1\propto}T^{1.2}$ for the Bi_2Te_3 below 270 K.

the T_1 properties is the SOC of the p-band electrons.[37,40,41,55] Ab initio calculations and ARPES results[33,36,40,41] suggest that the $Bi_{0.5}Sb_{1.5}Te_3$ compound has an increased *p*-band conductivity in bulk states compared to the binary parent compounds (Bi_2Te_3 and Sb_2Te_3).

In Figure 5 inset, we plot the quantity $1/(T_1.T^{0.5})$ which is proportional to the charge carrier concentration in a semiconductor (*N*)[54,56,59,61,68] The $Bi_{0.5}Sb_{1.5}Te_3$ follows a linear trend which is indicative of a metallic sample across the temperature range investigated. Figure 5c shows that the $Bi_{0.5}Sb_{1.5}Te_3$ and Sb_2Te_3 have almost three times higher carrier density than Bi_2Te_3 and more than seven times higher than Bi_2Te_2Se across all temperatures investigated. This plot confirms that Sb-TI samples are significantly more conductive than all other TI samples.

In **Figure 6**, we fitted T_1 from a saturation-recovery experiment for the phase separated Bi_2Te_2S at 355 K and room temperature for the central versus shoulder peaks and found significantly different T_1 values for each peak. We note that the shoulder peak relaxes 1.8 times faster than the central peak at both temperatures. This is an interesting result because by increasing the temperature, an even partial annealing effect would have been expected to show a gradual change in T_1 as opposed to the difference observed between the shoulder and central peaks. The PXRD patterns (Figure 1) do not provide evidence of any damage to the bulk, suggesting that the observed positive frequency shift peak is likely primarily a phase separation effect. ^{125}Te NMR line shape measurements in Bi_2Te_2S at 355K, as shown in Figure 6a, provide experimental evidence about the existence of two distinct regions (phase separation, see also Figure 1c). Furthermore, the NMR shoulder peak characteristics (frequency shift and linewidth) evolve with temperature in a way similar to "pure" Bi_2Te_3, as shown in Figure 3, which further supports the view that this material consists of two coexisting phases.

4. Conclusions

A variable temperature ^{125}Te NMR study has been performed on Bi_2Te_3, Sb_2Te_3, $Bi_{0.5}Sb_{1.5}Te_3$, Bi_2Te_2Se and Bi_2Te_2S, revealing fundamental differences between these five chalcogenides

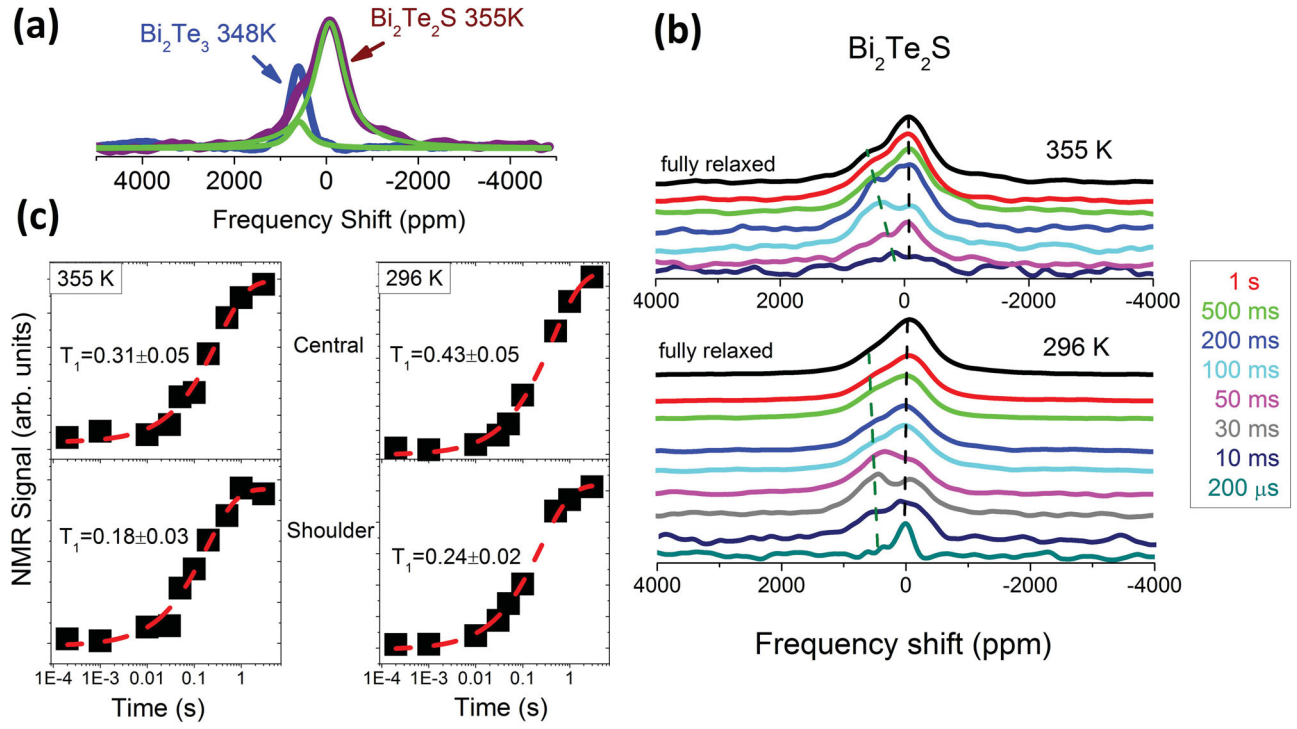

Figure 6. The ^{125}Te NMR spectra for the phase separated Bi_2Te_2S (purple line) at 355 K and Bi_2Te_3 (blue line) at 348 K. The green thin lines are the individual components of a two-Lorentzian fitting (a). The shoulder peak at more positive shifts of Bi_2Te_2S corresponds to the S-poor Bi_2Te_3 phase which is in agreement with the PXRD pattern analysis as shown in Figure 1c. Comparison of the ^{125}Te spectrum for the phase-separated Bi_2Te_2S at 355 K and 296 K obtained in the saturation recovery experiment after saturation of 200 µs to 3 s (b). Relaxation recovery is not uniform across the resonance. The regions at more positive shifts (shoulder peak) relax more quickly (c) than those at more negative shifts (central peak). The red line are fitted to a stretched exponential saturation-recovery model with the $\beta = 0.7$.

which originate from the presence of different defect content in the tetradymite matrix. Asymmetric static lineshapes due to a distribution of Knight shifts in various domains of the sample, arising from the presence of antisite defects as the substitutional component (Se, S or Sb in Bi_2Te_3 matrix) concentration increases. Relaxation studies show that the binary TIs exhibit different characteristics compared to the ternary sample suggesting a range of charge carrier densities due to an extensive distribution of defects. A lower thermal activation energy and a lower Korringa product accompanied by a stronger negative frequency shift suggest a more conductive bulk profile for $Bi_{0.5}Sb_{1.5}Te_3$ than the two parent binary TIs. On the other hand, Bi_2Te_2S and the ordered Bi_2Te_2Se maintain the lower values of $1/(T_1 \cdot T^{0.5}) \propto N$ featuring a more insulating behavior across the entire temperature range. This result is consistent with recent magneto-transport studies[1–6] of the bulk state resistivity; this is consistent with PXRD and NMR results in Table 1. We also provide an experimental evidence about the existence of two distinct regions in the Bi_2Te_2S composition. Due to the high sensitivity of the NMR technique to sample defects, homogeneity and carrier concentration, this study further supports previous reports asserting that the ordered ternary compound Bi_2Te_2Se is the best TI material among those investigated herein. This is because the bulk state remains insulating across the entire temperature range, allowing the surface states to dominate the material's conductivity.

5. Experimental Section

Materials: Sb_2Te_3 and Bi_2Te_3 ingots were purchased from Alfa Aesar, $Bi_{0.5}Sb_{1.5}Te_3$ from Sigma-Aldrich and used without further purification or recrystallization. According to the manufacturers, samples are grown in solid-state reactions by reacting elemental metals in a high temperature furnace to form ingots. Bi_2Te_2Se and Bi_2Te_2S ingots were synthesized by mixing the appropriate ratios of elemental Bi, Te, and Se/S. Tubes were sealed under high vacuum (~10^{-4} Torr), heated to 800 °C over 15 h, kept at 800 °C for 10 h, and cooled to room temperature over 15 h.

Structural, Electrical and Nuclear Magnetic Resonance Characterization: Powder X-ray diffraction (PXRD) analysis was carried out on a Panalytical X'Pert Pro X-ray Powder Diffractometer with Cu Kα radiation (λ = 1.54050 Å). Particle sizes reported for the samples are average particle sizes determined from PXRD data. For the commercial compositions, Bi_2Te_3, Sb_2Te_3 and $Bi_{0.5}Sb_{1.5}Te_3$, a range of carrier concentrations is given based on literature data. For the Bi_2Te_2Se and Bi_2Te_2S compositions, carrier concentrations were determined using measurements of Hall coefficients at room temperature with a home-built system in an applied magnetic field. For NMR studies, the ingots were ground by mortar and pestle. PXRD results as shown in Table 1 (lattice parameters) and in Figure 1b (indexing powder patterns) indicate that the samples remain crystalline after the mortar and pestle process. The PXRD studies indicate that the bulk is damage free. Damage to the edges probably exists, but is of no consequence here because we are probing the bulk of these materials (our powders are micrometer sized, so the surface-to-volume effects are negligible). ^{125}Te NMR data were acquired on static powder samples with a Bruker DSX-300 spectrometer operating at 94.79 MHz using a standard Bruker X-nucleus wideline probe with a 5-mm solenoid coil. The ^{125}Te $\pi/2$ pulse width in the wideline probe

was 4 μs. Spectral data were acquired using a spin-echo sequence [$\pi/2$) x – τ – π) y - acquire]. The echo delay, τ, was set to 20 μs. The spin-echo sequence is useful in minimizing pulse ringdown effects. In order to acquire the full ^{125}Te NMR spectrum of the samples, we used the variable offset cumulative spectra technique.[66] Data for determining the spin-lattice relaxation times (T_1) were acquired with the saturation-recovery technique. The ^{125}Te chemical shift scale was calibrated using the unified Ξ scale, relating the nuclear shift to the ^{1}H resonance of dilute tetramethylsilane in $CDCl_3$ at a frequency of 300.13 MHz.[67]

Acknowledgments

This research was supported by the Defense Advanced Research Project Agency (DARPA), Award No. N66001-12-1-4034. We acknowledge the use of instruments at the Molecular Instrumentation Center (MIC) facility at UCLA.

Received: August 7, 2013
Published online: December 4, 2013

[1] Z. Ren, A. Taskin, S. Sasaki, K. Segawa, Y. Ando, *Phys. Rev. B* **2010**, *82*, 241306(R).
[2] Z. Ren, A. Taskin, S. Sasaki, K. Segawa, Y. Ando, *Phys. Rev. B* **2012**, *85*, 155301.
[3] L. Wang, M. Huang, S. Thimmaiah, A. Alam, S. L. Bud'ko, A. Kaminski, T. A. Lograsso, P. Canfield, D. D. Johnson, *Phys. Rev. B* **2013**, *87*, 125303.
[4] S. Jia, H. Ji, E. Climent-Pascual, M.K. Fuccillo, M.E. Charles, J. Xiong, N. P. Ong, R.J. Cava, *Phys. Rev. B* **2011**, *84*, 235206.
[5] H. Ji, J. M. Allred, M. K. Fuccillo, M. E. Charles, M. Neupane, L. A. Wray, M. Z. Hasan, R. J. Cava, *Phys. Rev. B* **2012**, *85*, 201103(R).
[6] R. J. Cava, H. Ji, M. K. Fuccillo, Q. D. Gibson, Y. S. Horb, *J. Mater. Chem. C* **2013**, DOI: 10.1039/C3TC00587A.
[7] T. M Tritt, M. A. Subramanian, *MRS Bulletin* **2011**, *31*, 188.
[8] G. J. Snyder, E. S. Toberer, *Nat. Mater.* **2008**, *7*, 105–14.
[9] M. Kanatzidis, *Chem. Mater.* **2010**, *22*, 648.
[10] D. M. Rowe, *CRC Handbook of Thermoelectrics*, CRC Press, NewYork, USA **1995**.
[11] M. Z. Hasan, C. L. Kane, *Rev. Modern Phys.* **2010**, *82*, 3045.
[12] Y. Xia, D. Qian, D. Hsieh, L. Wray, A. Pal, H. Lin, A. Bansil, D. Grauer, Y. S. Hor, R. J. Cava, M. Z. Hasan, *Nature Phys.* **2009**, *5*, 398.
[13] J. Cha, K. Koski, Y. Cui, *Phys. Status Solidi* **2013**, *7*, 15.
[14] F.-T. Huang, M.-W. Chu, H. H. Kung, W. L. Lee, R. Sankar, S.-C. Liou, K. K. Wu, Y. K. Kuo, F. C. Chou, *Phys. Rev. B* **2012**, *86*, 081804(R).
[15] J. E. Moore, L. Balents, *Phys. Rev. B* **2007**, *75*, 121306.
[16] H. Zhang, C.-X. Liu, X.-L. Qi, X. Dai, Z. Fang, S.-C. Zhang, *Nature Phys.* **2009**, *5*, 438.
[17] Y. Lan, B. Poudel, Y. Ma, D. Wang, M. S. Dresselhaus, G. Chen, Z. Ren, *Nano Lett.* **2009**, *9*, 1419.
[18] J. Fleurial, L. Gailliard, R. Triboulet, H. Scherrer, S. Scherrer, *J. Phys. Chem. Solids* **1988**, *49*, 1237.
[19] J. Horák, Z. Starý, P. Loštak, J. Panci , *J. Phys. Chem Solids* **1990**, *51*, 1353.
[20] D. Kraemer, B. Poudel, H. Feng, C. Caylor, B. Yu, X. Yan, Y. Ma, X. Wang, D. Wang, A. Muto, K. McEnaney, M. Chiesa, Z. Ren, G. Chen, *Nature Mater.* **2011**, *10*, 532.
[21] S. Walia, R. Weber, S. Sriram, M. Bhaskaran, K. Latham, S. Zhuiykov, K. Kalantar-zadeh, *Energy Environ. Sci.* **2011**, *4*, 3558.
[22] P. Yu, M. Cardona, *Fundamentals of Semiconductors: Physics and Materials Properties*. Springer, New York, USA **1999**.
[23] M. M. Ibrahim, M. M. Wakkad, E. Kh. Shokr, H. A. Abd EI-Ghani, *Appl. Phys. A* **1991**, *52*, 237.
[24] B. Poudel, Q. Hao, Y. Ma, Y. Lan, A. Minnich, B. Yu, X. Yan, D. Wang, A. Muto, D. Vashaee, X. Chen, J. Liu, M. S. Dresselhaus, G. Chen, Z. Ren, *Science* **2008**, *320*, 634.
[25] C. H. Champness, P. T. Chiang, P. Parekh, *Can. J. Phys.* **1965**, *43*, 653.
[26] W. M. Yim, E. V. Fitzke, *J. Electrochem. Soc.* **1968**, *115*, 556.
[27] V. Das, N. Soundararajan, *J. Appl. Phys.* **1989**, *65*, 2332.
[28] K. Park, S. W. Nam, C. H. Lim, *Intermettalics* **2010**, *18*, 1744.
[29] X. Li, E. Koukharenko, I. Nandhakumar, J. Tudor, S. P. Beeby, N. M. White, *Phys. Chem. Chem. Phys.* **2009**, *11*, 3584.
[30] A. Hruban, A. Materna, W. Dalecki, G. Strzelecka, M. Piersa, E. Jurkiewicz-Wegner, R. Diduszko, M. Romaniec, W. Orłowski, *Acta Phys. Polon. A* **2011**, *120*, 950.
[31] M. Stordeur, W. Heiliger, *Phys. Status Solidi* **1976**, *78*, 103.
[32] R. Makala, K. Jagannadham, B. C. Sales, H. Wang, *Mat. Res. Soc. Symp. Proc.* **2002**, *691*, G8.4.1.
[33] A. N. Veis, *Russian Phys. J.* **2008**, *51*, 714.
[34] C. B. Satterthwaite, R. W. Ure, *Phys. Rev.* **1957**, *108*, 1164.
[35] D. A. Wright, *Nature* **1958**, *181*, 834.
[36] S. K. Mishra, S. Satpathy, O. Jepsen, *J. Phys. Cond. Matt.* **1997**, *9*, 461.
[37] L.-L. Wang, D. D. Johnson, *Phys. Rev. B* **2011**, *83*, 241309.
[38] S.-Y. Xu, L. A. Wray, Y. Xia, R. Shankar, A. Petersen, A. Fedorov, H. Lin, A. Bansil, Y. S. Hor, D. Grauer, R. J. Cava, M. Z. Hasan, **2010**, arXiv:1007.5111.
[39] D. O. Scanlon, P. D. C. King, R. P. Singh, A. de la Torre, S. M. Walker, G. Balakrishnan, F. Baumberger, C. R. A. Catlow, *Adv. Mater.* **2012**, *24*, 1254.
[40] D. Kong, Y. Chen, J. J. Cha, Q. Zhang, J. G. Analytis, K. Lai, Z. Liu, S. S. Hong, K. J. Koski, S.-K. Mo, Z. Hussain, I. R. Fisher, Z.-X. Shen, Y. Cui, *Nature Nanotechnol.* **2011**, *6*, 705.
[41] J. Zhang, C.-Z. Chang, Z. Zhang, J. Wen, X. Feng, K. Li, M. Liu, K. He, L. Wang, X. Chen, Q.-K. Xue, X. Ma, Y. Wang, *Nature Comm.* **2011**, *2*, 574.
[42] S. Urazhdin, D. Bilc, S. H. Tessmer, S. D. Mahanti, T. Kyratsi, M. G. Kanatzidis, *Phys. Rev. B* **2002**, *66*, 161306-1(R).
[43] S. Urazhdin, D. Bilc, S. D. Mahanti, S. H. Tessmer, T. Kyratsi, M. G. Kanatzidis, *Phys. Rev. B* **2004**, *69*, 85313.
[44] S. Misra, G. S. Tripathi, P. K. Misra, *J. Phys. C: Solid State Phys.* **1987**, *20*, 277.
[45] R. E. Watson, L. H. Bennett, G. C. Carter, I. D. Weisman, *Phys. Rev. B* **1971**, *3*, 222.
[46] T. P. Das, E. H. Sondheimer, *Phil. Mag.* **1960**, *5*, 529.
[47] H. M. Vieth, S. Vega, N. Yellin, D. Zamir, *J. Phys. Chem.* **1991**, *95*, 1420.
[48] B. Y. Yavorsky, N. F. Hinsche, I. Mertig, P. Zahn, *Phys. Rev. B* **2011**, *84*, 165208.
[49] B. G. Martin, L. S. Lerner, *Phys. Rev. B* **1972**, *6*, 8.
[50] H.-W. Jeon, H.-P. Ha, D.-B. Hyn, J.-D. Shim, *J. Phys. Chem. Solids* **1991**, *52*, 4.
[51] H. Noh, H. Koh, S. Oh, J. Park, H. Kim, J. D. Rameau, T. Valla, T. E. Kidd, P. D. Johnson, Y. Hu, Q. Li, *Europhys. Lett.* **2008**, *81*, 57006.
[52] M. Romanowich, M.–S. Lee, D.–Y. Chung, S. D. Mahanti, M. G. Kanatzidis, S. H. Tessmer, *Phys. Rev. B* **2013**, *87*, 085310.
[53] H. B. Zhang, H. L. Yu, G. W. Yang, *Eur. Phys. Lett.* **2011**, *95*, 56002.
[54] D. Koumoulis, T. C. Chasapis, R. E. Taylor, M. P. Lake, D. King, N. N. Jarenwattananon, G. A. Fiete, M. G. Kanatzidis, L. S. Bouchard, *Phys. Rev. Lett.* **2013**, *110*, 026602.
[55] R. E. Taylor, B. Leung, M. P. Lake, L. S. Bouchard, *J. Phys. Chem. C* **2012**, *116*, 17300.
[56] B.-L. Young, Z.-Y. Lai, Z. Xu, A. Yang, G.-D. Gu, Z.-H. Pan, T. Valla, G. J. Shu, R. Sankar, F. C. Chou, *Phys. Rev. B* **2012**, *86*, 075137.
[57] D. M. Nisson, A. P. Dioguardi, P. Klavins, C. H. Lin, K. Shirer, A. C. Shockley, J. Crocker, N. J. Curro, *Phys. Rev. B* **2013**, *87*, 195202.
[58] A. M. Panich, M. Shao, C. L. Teske, W. Bensch, *Phys. Rev. B* **2006**, *74*, 233305.

[59] J. P. Yesinowski, *Top. Curr. Chem.* **2012**, *306*, 229.
[60] J. P. Yesinowski, A. P. Purdy, H. Wu, M. G. Spencer, J. Hunting, F. J. DiSalvo, *J. Am. Chem. Soc.* **2006**, *128*, 4952.
[61] R. Taylor, F. Alkan, D. Koumoulis, M. Lake, D. King, C. Dybowski, L. S. Bouchard, *J. Phys. Chem. C* **2013**, *117*, 8959.
[62] D. West, Y. Y. Sun, H. Wang, J. Bang, S. B. Zhang, *Phys. Rev. B* **2012**, *86*, 121201(R).
[63] A. E. Kar'kin, V. V. Shchennikov, B. N. Goshchitskiœ, S. E. Danilov, V. L. Arbuzov, V. A. Kul'bachinskiœ, *Phys. Solid State* **2003**, *45*, 2249.
[64] V. A. Kulbachinskii, V. G. Kytin, A. A. Kudryashov, P. M. Tarasov, *AIP Conf. Proc.* **2012**, *1449*, 119.
[65] P. Dutta, D. Bhoi, A. Midya, N. Khan, P. Mandal, S. Shanmukharao Samatham, V. Ganesan, *Appl. Phys. Lett.* **2012**, *100*, 251912.
[66] D. Massiot, I. Farnan, N. Gautier, D. Trumeau, A. Trokiner, J. P. Coutures, *Solid State Nucl. Magn. Reson.* **1995**, *4*, 241.
[67] R. K. Harris, E. D. Becker, S. M. Cabral de Menezes, R. Goodfellow, P. Granger, *Pure Appl. Chem.* **2001**, *73*, 1795.
[68] K. Ooiwa, K. Endo, *J. Magn. Magn. Mat.* **1998**, *177*, 1443.
[69] A. Boulouz, S. Chakraborty, A. Giani, F. P. Delannoy, A. Boyer, J. Schumann, *J. Appl. Phys.* **2001**, *89*, 5009.
[70] P. Lostak, J. Horak, *Physica Scripta* **1988**, *37*, 812.
[71] W. Liu, K. C. Lukas, K. McEnaney, S. Lee, Q. Zhang, C. P. Opeil, G. Chen, Z. Ren, *Energy Environ. Sci.* **2013**, *6*, 552.
[72] D. C. Grauer, Y. S. Hor, A. J. Williams, R. J. Cava, *Mat. Res. Bull.* **2009**, *44*, 1926.
[73] D. C. Johnston, *Phys. Rev. B* **2006**, *74*, 184430.
[74] S. Tongay, J. Zhou, C. Ataca, K. Lo, T. S. Matthews, J. Li, J. C. Grossman, J. Wu, *Nano Lett.* **2012**, *12*, 5576.
[75] Y. Kim, X. Chen, Z. Wang, J. Shi, I. Miotkowski, Y. P. Chen, P. A. Sharma, A. L. Lima Sharma, M. A. Hekmaty, Z. Jiang, D. Smirnov, *Appl. Phys. Lett.* **2012**, *100*, 071907.
[76] X. Chen, H. D. Zhou, A. Kiswandhi, I. Miotkowski, Y. P. Chen, P. A. Sharma, A. L. Lima Sharma, M. A. Hekmaty, D. Smirnov, Z. Jiang, *Appl. Phys. Lett.* **2011**, *99*, 261912.
[77] G. E. Shoemake, J. A. Rayne, R. W. Ure, *Phys. Rev.* **1969**, *185*, 1046.
[78] A. Koma, A. Hojo, S. Tanaka, *Phys. Lett. A* **1968**, *28*, 2.
[79] L.-S. Bouchard, A. O. Sushkov, D. Budker, J. J. Ford, A. S. Lipton, *Phys. Rev. A* **2008**, *77*, 022102.
[80] B. Günther, O. Kanert, *Phys. Rev. B* **1985**, *31*, 20.
[81] G. Neue, S. Bai, R. E. Taylor, P. A. Beckmann, A. J. Vega, C. Dybowski, *Phys. Rev. B* **2009**, *79*, 214302.
[82] L. Hu, H. Gao, X. Liu, H. Xie, J. Shen, T. Zhu, X. Zhao, *J. Mater. Chem.* **2012**, *22*, 16484.